

SCIENTIFIC REPORTS



OPEN

THz-circuits driven by photo-thermoelectric, gate-tunable graphene-junctions

Andreas Brenneis^{1,2}, Felix Schade^{1,2}, Simon Drieschner^{1,2}, Florian Heimbach^{2,3}, Helmut Karl⁴, Jose A. Garrido^{1,2} & Alexander W. Holleitner^{1,2}

Received: 21 June 2016
Accepted: 03 October 2016
Published: 20 October 2016

For future on-chip communication schemes, it is essential to integrate nanoscale materials with an ultrafast optoelectronic functionality into high-frequency circuits. The atomically thin graphene has been widely demonstrated to be suitable for photovoltaic and optoelectronic devices because of its broadband optical absorption and its high electron mobility. Moreover, the ultrafast relaxation of photogenerated charge carriers has been verified in graphene. Here, we show that dual-gated graphene junctions can be functional parts of THz-circuits. As the underlying optoelectronic process, we exploit ultrafast photo-thermoelectric currents. We describe an immediate photo-thermoelectric current of the unbiased device following a femtosecond laser excitation. For a picosecond time-scale after the optical excitation, an additional photo-thermoelectric contribution shows up, which exhibits the fingerprint of a spatially inverted temperature profile. The latter can be understood by the different time-constants and thermal coupling mechanisms of the electron and phonon baths within graphene to the substrate and the metal contacts. The interplay of the processes gives rise to ultrafast electromagnetic transients in high-frequency circuits, and it is equally important for a fundamental understanding of graphene-based ultrafast photodetectors and switches.

Graphene is a gapless broadband absorber, which allows to detect wavelength-multiplexed signals in the frequency range from THz to UV-Vis-radiation¹. In particular, free-charge carrier excitations can be exploited for THz signal propagation², whereas interband excitations, like photogenerated electron-hole pairs, can drive ultrafast currents because of a femtosecond relaxation of photogenerated charge-carriers. A corresponding ultrafast photovoltaic current is driven by built-in electric fields, for instance, at metal-graphene junctions^{3–7} and by an externally applied bias voltage⁸. An alternative route to harvest and exploit the energy of incident photons are so-called photo-thermoelectric currents, which have been reported for graphene *p-n* junctions^{9–13}, junctions made from mono- and bilayer graphene¹⁴, and graphene junctions with asymmetric metal contacts¹⁵. The thermopower differs on the two adjacent sides of these junctions, and the optical excitation generates the necessary heat to drive the thermoelectric current. Graphene is particularly suited to host thermoelectric currents, because the electron-electron scattering is the dominant ultrafast decay channel for a low irradiation intensity¹⁶. In turn, a hot electron distribution can quickly form after the optical excitation with only a small dissipation to the crystal lattice^{13,17–19}. Hereby, non-equilibrium charge carrier temperatures of 10^3 – 10^4 K can be achieved^{16,20}. Such an elevated temperature in combination with the large thermopower of graphene ($\approx 100 \mu\text{V/K}$) gives rise to a significant photo-thermoelectric response. As it is shown here, the latter can be used for triggering ultrafast signals in high-frequency circuits.

We exploit an on-chip pump-probe photocurrent spectroscopy based on THz-waveguides and Auston-switches with a sub-picosecond time-resolution^{7,21–23}. Our technique can detect photocurrents that are linear with respect to the laser power^{13,16}, and moreover, we detect signals which trigger electromagnetic transients in the THz circuits^{21,24,25}. We can distinguish two ultrafast contributions in the graphene-junctions. On the one hand, an immediate response occurs during the pulsed excitation. This immediate response exhibits a six-fold sign-change as a function of both gate voltages of the dual-gated junction. This is a clear finger-print of a

¹Walter Schottky Institut and Physics Department, Technical University Munich, Am Coulombwall 4a, 85748 Garching, Germany. ²Nanosystems Initiative Munich (NIM), Schellingstr. 4, 80799 Munich, Germany. ³Lehrstuhl für Physik funktionaler Schichtsysteme, Physics Department, Technical University of Munich, D-85748 Garching, Germany. ⁴Institute of Physics, University of Augsburg, 86135 Augsburg, Germany. Correspondence and requests for materials should be addressed to A.W.H. (email: holleitner@wsi.tum.de)

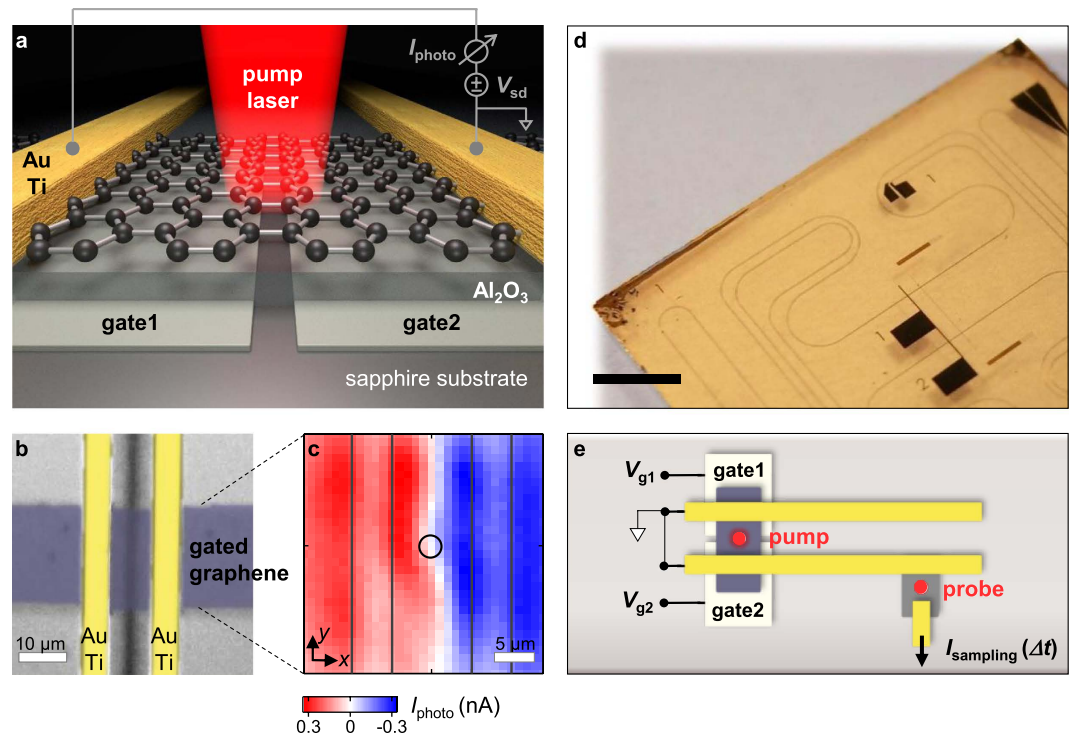


Figure 1. Gated graphene-junction integrated in a THz circuit. (a) Sketch of a dual-gated graphene junction with two bottom gates, named gate1 and gate2, on top of a sapphire substrate and an insulating Al₂O₃-layer in-between. The graphene is contacted by two Ti/Au-striplines. A pulsed laser generates charge carriers in the graphene. (b) Microscope image of a corresponding graphene sheet (highlighted in blue) and the striplines (yellow) on top of two gates. The lateral gap between both gates is $\approx 2 \mu\text{m}$ (dark region in the center). (c) Spatially resolved and time-integrated photocurrent I_{photo} of the graphene sheet shown in Fig. 1b as a function of the coordinates x and y . For $x = y = 0 \mu\text{m}$, the sample is excited at the position of the circle. The vertical contour lines depict the positions of the striplines. (d) Image of the overall THz-stripline circuit on a sapphire chip. Scale bar, 2 mm. (e) Sketch of the on-chip pump/probe scheme. A pump pulse excites the gated graphene-junction, while the probe pulse triggers an Auston-switch. The latter is an ultrafast photoswitch and it reads out the electromagnetic transients of the striplines. As a function of the time-delay Δt , the corresponding current I_{sampling} gives insights into the electromagnetic signals running along the high-frequency striplines and hereby, into the temporal optoelectronic dynamics of the graphene-junction.

photo-thermoelectric current^{9,11,19}. On the other hand, we observe a decaying photocurrent contribution on the time-scale of a few picoseconds. We can numerically compute this decaying response by a thermoelectric current which is driven by an inverted temperature profile within the graphene device. The non-equilibrium temperature inversion occurs because the electron and phonon baths of the graphene couple differently to the metal contacts and to the underlying substrate of the device. Our results show that the heat loss to the immediate environment of the graphene plays an important role in optimizing the energy conversion efficiency in graphene. The insights into the non-equilibrium carrier dynamics may prove essential for future ultrafast optoelectronic switches and for the fundamental understanding of photovoltaic devices and photodetectors. In particular, our work experimentally proves that photo-thermoelectric currents can be used for an ultrafast optoelectronic signal-conversion in graphene as a functional part of high-frequency circuits^{26,27}. We show how dual-gated graphene junctions can be designed and fabricated such that they drive on-chip THz-circuits. Since graphene junctions can act as very efficient far-field THz-detectors¹⁵, our work on gate-tunable, photo-thermoelectric graphene-junctions suggest that they can act as off/on-chip interconnects in the THz-regime.

Results

Sample Fabrication. Figure 1a sketches the sample layout of the dual-gated graphene junction. The circuit provides two gates labeled gate1 and gate2. Applying corresponding gate voltages V_{g1} and V_{g2} controls the Fermi levels and thus the thermopower in the graphene on each side of the junction. The graphene is electrically contacted by metal strips made from Ti/Au (10 nm/250 nm), which allow to apply a bias voltage V_{sd} . First, two adjacent 10 nm thick Pt gates are lithographically defined on a sapphire substrate. Then, a 30 nm thick, ALD-grown (atomic layer deposition) Al₂O₃-layer isolates the gates from the graphene. Subsequently, CVD-grown (chemical vapor deposition) graphene is mechanically transferred to the sample²⁸. The graphene region of interest is 25 μm wide and meanwhile protected with a resist, while the remaining graphene is removed by utilizing an oxygen plasma. In a final lithography step, the protective resist is removed by a solvent, and the striplines are lithographically defined on top of the graphene. Figure 1b shows an optical microscope image of the device with the

graphene (striplines) being highlighted in blue (yellow). The gap between the two underlying Pt-gates is clearly visible as dark contrast. Moreover, the Ti/Au-contacts form coplanar high-frequency striplines with a total length of ≈ 44 μm , a width of 5 μm , and a separation of 10 μm . The striplines are needed to measure the time-resolved photocurrent I_{sampling} ^{7,21}.

Scanning photocurrent microscopy. For the excitation of the graphene, we use a laser system that emits laser pulses with a 30 fs pulse duration at a repetition rate of 80 MHz in the spectral range from 900 to 1500 nm (cf. Supplementary Figure S1). The laser beam is focused with a 15x reflective objective. The laser spot on the surface of the graphene has a full width half maximum (FWHM) of ≈ 5.5 μm . All presented experiments are performed with an excitation power of 1–2 mW at room temperature and in a vacuum chamber. First, the time-integrated photocurrent I_{photo} is measured with the help of a current-voltage amplifier while the sample is scanned laterally by the help of piezoelectric positioners. Figure 1c depicts such a photocurrent map of I_{photo} at $V_{\text{sd}} = V_{\text{g1}} = V_{\text{g2}} = 0\text{V}$. For these experimental parameters, I_{photo} shows opposite signs on both sides of the junction, as it will be discussed below.

THz-time domain photocurrent spectroscopy. For measuring the ultrafast optoelectronic dynamics of the graphene-based junction, we use an on-chip THz-time domain photocurrent spectroscopy of the stripline circuits (Fig. 1d)^{7,21–23}, where an optical femtosecond pump laser excites the charge carriers in the graphene (Fig. 1e). This laser is the same as for the time-integrated photocurrent measurements (Fig. 1a). Since the contacts form striplines, the photocurrents give also rise to electromagnetic transients in the metal striplines with a bandwidth of up to 2 THz^{21,22}. The transients run along the striplines, and they are detected on-chip by a time-delayed optical femtosecond probe pulse in combination with an Auston-switch (Fig. 1e)²¹. We use ion-implanted amorphous silicon for this ultrafast photodetector with a time-resolution of about 1 ps^{22,23}. The probe pulse has a photon energy of 1.59 eV and a temporal width of 100 fs. The current I_{sampling} across the Auston-switch samples the electromagnetic transients on the striplines as a function of the time-delay Δt between the two laser pulses, and it is directly proportional to the ultrafast photocurrents in the graphene. Hereby, the photocurrents in the graphene can be measured with a picosecond time-resolution^{7,21}.

Resistance properties of the graphene junction. The two-terminal resistance R_{total} is measured with a current-voltage amplifier to gain insights into the electronic properties of the dual-gated graphene junction. Figure 2a shows the experimental dependence of R_{total} , when both voltages of gate1 and gate2 are varied simultaneously. We find the charge neutrality point of the graphene for negative gate voltages ($V_{\text{d}} < 0\text{V}$), which implies that it is intrinsically *n*-doped. Figure 2b shows R_{total} , when V_{g1} and V_{g2} are varied independently. We apply the following model²⁹ to approximate the charge carrier density in dependence of the applied gate voltage

$$n(V_{\text{g}}) \approx \sqrt{n_{\text{ind}}^2(V_{\text{g}}) + n_0^2} = n_0 \sqrt{\left(\frac{V_{\text{g}} - V_{\text{d}}}{\Delta}\right)^2 + 1}. \quad (1)$$

Here, n_0 is the residual charge carrier density (*i.e.* the minimum sheet carrier concentration), n_{ind} the gate-induced charge carrier density, n the total charge carrier density. The term Δ is defined as $\Delta = \frac{n_0 e}{C^*}$, with C^* the specific capacitance $C^* = \frac{\epsilon_0 \epsilon_r}{d}$ of the gate and the graphene-sheet²⁹ (with $\epsilon_r = 6.0$ the relative permittivity and $d = 30$ nm the thickness of the Al_2O_3 layer). The data in Fig. 2b can be fitted by

$$R_{\text{total}}(V_{\text{g1}}, V_{\text{g2}}) = R_{\text{contact}} + R_{\text{g1}}(V_{\text{g1}}) + R_{\text{g2}}(V_{\text{g2}}), \quad (2)$$

The expression R_{contact} accounts for the constant resistance of the metal striplines and the ungated graphene region. R_{gi} represents the gate voltage dependent resistance of the two ($i = 1, 2$) gated graphene sections, respectively. This resistance is related to the conductivity by $R_{\text{gi}} = \frac{l}{w\sigma_i}$, where $l = 4$ μm and $w = 25$ μm are the length and width of the gated graphene sections, respectively. The conductivity $\sigma_i(V_{\text{gi}})$ can be tuned by the gate voltage V_{gi} and is calculated from $\sigma_i = e \cdot \mu_i \cdot n_i(V_{\text{gi}})$ using Eq. (1). Our fit gives $R_{\text{contact}} = 2.57$ k Ω and mobilities of $\mu_1 = 157$ $\text{cm}^2\text{V}^{-1}\text{s}^{-1}$ and $\mu_2 = 278$ $\text{cm}^2\text{V}^{-1}\text{s}^{-1}$. The charge neutrality point is reached at $V_{\text{d1}} = -1.92$ V and $V_{\text{d2}} = -2.77$ V. The fit further reveals $\Delta_1 = 3.20$ V and $\Delta_2 = 2.62$ V. Figure 2c shows the resulting fit (cf. Supplementary Figures S2 and S3).

Photo-thermoelectric properties. The photo-thermoelectric effect^{9–11,19} and the photovoltaic effect^{3,4,6–8} are considered as the two distinctive photocurrent generation mechanisms in graphene on short time-scales. The photovoltaic effect relies on a drift current, where photogenerated charge carriers are separated by an electric field. In turn, the photovoltaic current monotonically depends on the difference of the Fermi levels of both sides of a dual-gated graphene junction (cf. Supplementary Figure S4). In the case of a thermoelectric generation mechanism, the photocurrent is a non-monotonic function. In particular, the thermoelectric voltage V_{TE} can be written as

$$V_{\text{TE}} = \int \frac{\partial T}{\partial x} \cdot S(x) \cdot dx = \sum_i \Delta T_i \cdot S_i(V_{\text{gi}}) = \Delta T \cdot [S_{\text{g1}}(V_{\text{g1}}) - S_{\text{g2}}(V_{\text{g2}})], \quad (3)$$

with ΔT_i the change in electron temperature for a segment with constant thermopower S_i . We define the x -axis as in Fig. 1c. The expression can be simplified to the last term of Eq. (3) for a symmetric heat profile with amplitude ΔT and for constant thermopowers S_{g1} and S_{g2} for the two areas on top of gate1 and gate2. We note that a

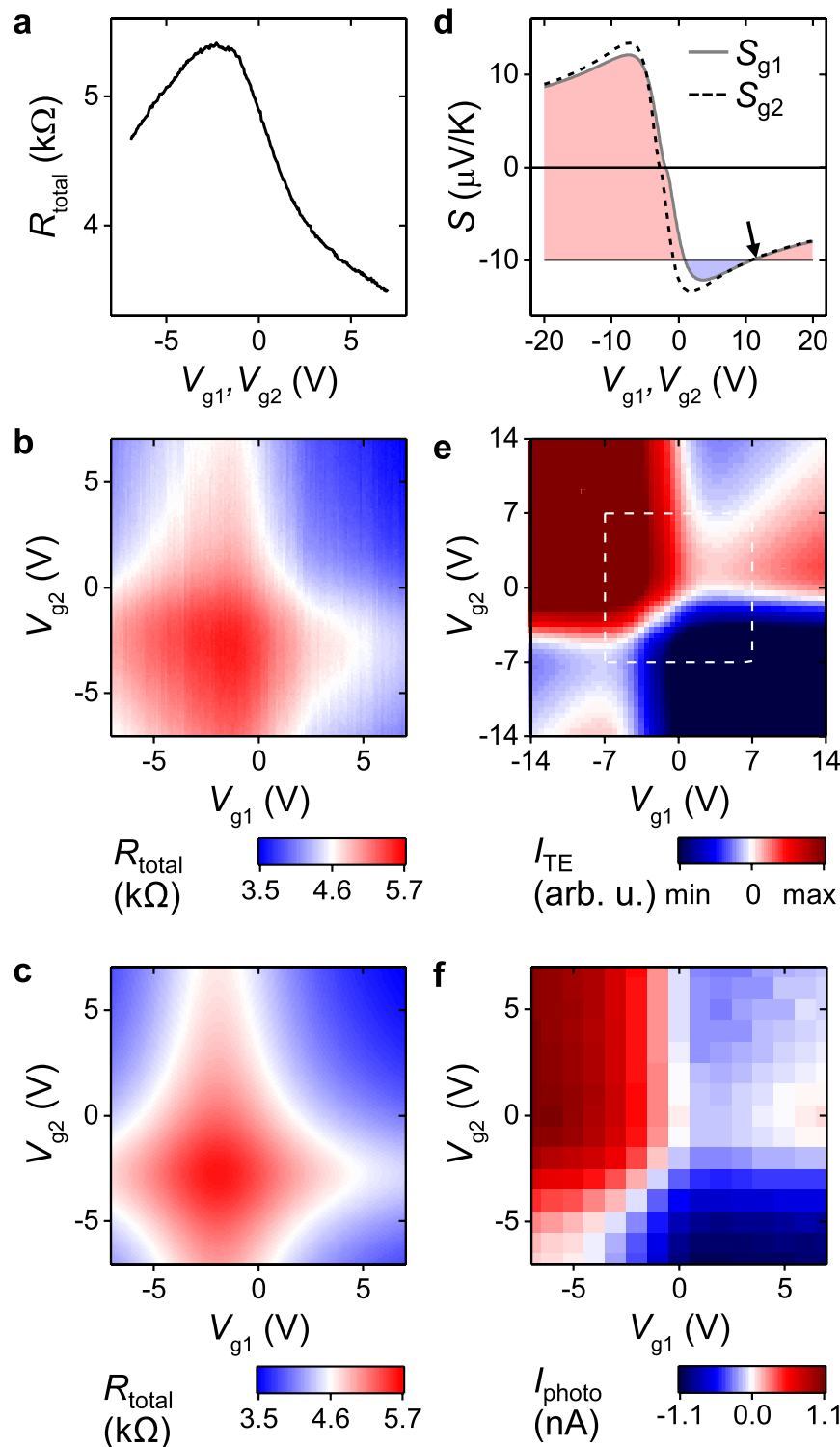


Figure 2. Electronic and photo-thermoelectric properties of the graphene-junction. (a) Two-terminal resistance R_{total} of the dual-gated graphene junction, when the two gate voltages V_{g1} and V_{g2} are swept simultaneously. The maximum gives the charge neutrality point of the graphene sheet. (b) Two-dimensional resistance plot $R_{\text{total}} = R_{\text{total}}(V_{g1}, V_{g2})$, when the gates are varied individually. (c) Two-dimensional fit of R_{total} according to Eq. (2). See text for details. (d) Seebeck coefficient S_{g1} (S_{g2}) vs. V_{g1} (V_{g2}) calculated from the fit parameters of R_{total} according to Eq. (5). (e) Calculated thermoelectric current vs. V_{g1} (V_{g2}) for the doping and mobility parameters from (c) according to Eq. (3) and $I_{\text{TE}} = V_{\text{TE}}/R_{\text{total}}$. (f) Experimental time-integrated photocurrent I_{photo} vs. V_{g1} (V_{g2}) at $x = y = 0$ (circle in Fig. 1c).

symmetric heat profile is introduced by the laser pulse with the given FWHM of $\approx 5.5 \mu\text{m}$ (Fig. 1a). The thermopower or so-called Seebeck coefficient can be related to the electric properties of the device following the Mott formula³⁰.

$$S = -\frac{\pi k_B^2 T_0}{3e} \cdot \frac{1}{\sigma} \frac{\partial \sigma}{\partial E} \Big|_{E=E_F} = \frac{\pi k_B^2 T_0}{3e} \cdot \frac{1}{R} \cdot \frac{\partial R_{\text{total}}}{\partial E} \Big|_{E=E_F}, \quad (4)$$

with E_F the Fermi-energy, k_B the Boltzmann constant, e the elementary charge, σ the electric conductivity, and $T_0 = 300 \text{ K}$ the equilibrium electron temperature. With the definitions from Eq. (1) and $E_F = \pm \hbar v_F \sqrt{\pi |n_{\text{ind}}|}$, Eq. (4) can be rewritten for each gate voltage

$$S_{gi} = \frac{2k_B^2 T_0}{3R_{\text{total}} \hbar v_F} \cdot \sqrt{\frac{\pi}{e C^*}} \cdot |V_{gi} - V_{di}| \cdot \frac{\partial R_{\text{total}}}{\partial V_{gi}} \quad (i = 1, 2). \quad (5)$$

Equation (5) is used to calculate the thermopower (Seebeck coefficients) $S_{gi} = S_{gi}(V_{gi})$ from the fit of $R_{\text{total}} = R_{\text{total}}(V_{g1}, V_{g2})$ in Fig. 2c. Figure 2d allows to intuitively understand the non-monotonic behavior of the thermopower as a function of V_{g1} and V_{g2} : for a given gate voltage V_{g2} and Seebeck coefficients S_{g2} (black arrow in Fig. 2d), there are two possible gate voltages V_{g1} , which result in a coincident Seebeck coefficient $S_{g1} = S_{g2}$. In turn, the thermoelectric current will show two crossing points as a function of V_{g1} and V_{g2} according to the right-hand-side of Eq. (3). The resulting six-fold sign change is therefore a characteristic, non-monotonic fingerprint of a thermoelectric current (Fig. 2e)^{9,11,19}. In the calculus, the gate voltages are varied from -14 to $+14 \text{ V}$. Experimentally, the breakdown voltage of the Al_2O_3 -layer limits the maximum sweeping range to $\pm 7 \text{ V}$ (dashed square in Fig. 2e). Figure 2f presents the corresponding time-integrated photocurrent I_{photo} of the dual-gated junction as a function of V_{g1} and V_{g2} , when the exciting laser is focused onto the center of the graphene junction (circle in Fig. 1c). Given the limited gate sweeping range, we clearly observe the sign change as expected from the pattern of the calculated thermoelectric current in Fig. 2e.

Ultrafast currents in the graphene-junction. In the following, we discuss the temporal dynamics of the non-equilibrium photocurrents in the graphene junction as detected by the THz stripline circuit. Figure 3a depicts the time-resolved photocurrent $I_{\text{sampling}}(\Delta t)$ for different gate voltages V_{g1} and V_{g2} . The voltage settings are defined by the indices in Fig. 3b. The signal can be described by a ‘peak current’ as an immediate response (green area in Fig. 3a), that occurs when the delay Δt between pump and probe pulse is zero. For a longer time-delay, we observe a rising and decaying behavior of I_{sampling} (gray area). We label the latter response as ‘decay current’. For each gate voltage setting, we fit $I_{\text{sampling}}(\Delta t)$ with a constant offset, a Lorentzian (green area), and an exponentially rising and decaying function $\propto \left(\exp\left[\frac{-\Delta t}{\tau_{\text{decay}}}\right] - \exp\left[\frac{-\Delta t}{\tau_{\text{rise}}}\right] \right)$ (gray area). The latter is a phenomenological function to describe the form of the decay current with rise and decay times τ_{decay} and τ_{rise} ²¹. They will be discussed below. The temporal width of the Lorentzian is $1.28 \pm 0.18 \text{ ps}$, which coincides with the bandwidth limitation of the present stripline circuit³¹. The bandwidth is limited by the dispersion and attenuation of the striplines. The dependences of the peak and decay currents on the gate voltages are depicted in Fig. 3b,c, respectively. The peak current exhibits a manifold sign change, which is in agreement with a thermoelectric current within the limited gate voltage range (compare to the highlighted square in Fig. 2e). The decay current rather depends on V_{g2} than on V_{g1} for this laser position. We further note that the peak current and the decay current can have different polarities at certain gate voltages (e.g. setting 1, 3, and 4 in Fig. 3a). At the given signal-to-noise-ratio, however, the sum of the peak and decay current (Fig. 3d) mimics the time-integrated signal I_{photo} (Fig. 2f) to a better extend than the peak current alone (Fig. 3b). This finding is consistent with the fact that the time-integrated signal comprises the sum of all ultrafast currents.

Discussion

We note that we read-out the ultrafast photocurrent results with a picosecond time-resolution in an on-chip manner only because of the split-gate design as sketched in Fig. 1a. For a global back gate which spans below one stripline to the other, the high-frequency components of the striplines are damped-out. A design guideline for the integration of gate-tunable graphene-junctions into THz-circuits is given in the Supplementary Note (Supplementary Figures S5–S10).

In order to explain the measured ultrafast peak and the decay currents in Fig. 3, we consider the ultrafast charge carrier relaxation dynamics. After the pulsed excitation, the charge carriers relax due to electron-electron scattering on a femtosecond time-scale, and the carrier ensemble can quickly be described by a hot Fermi-Dirac distribution^{13,16,19,32–36}. The electron and phonon bath temperatures equilibrate on a picosecond time-scale^{13,17–19} due to optical phonon scattering^{37,38}, surface polar phonon scattering^{39,40}, and supercollision scattering^{41–43}. From the striking similarity of the expected pattern of the thermoelectric current in Fig. 2e and the measured dependence of the ‘peak current’ in Fig. 3b, we can conclude that this immediate photocurrent is dominated by an ultrafast thermoelectric current at the junction. The necessary non-equilibrium electron temperature can be assumed to be as high as 10^4 K ^{16,20}. We find that it is important to excite at the center of the dual-gated junction such that a symmetric heat profile is impinged by the Gaussian laser profile with its given FWHM (sketch in Fig. 1a and circle in Fig. 1c). Hereby, the balanced temperature profile ($|\Delta T_1| = |\Delta T_2| = |\Delta T|$) and the difference in the thermopowers on both sides of the graphene give rise to a thermoelectric voltage $V_{\text{TE}} = (S_{g1} - S_{g2}) \Delta T$, that drives a photocurrent as long as the temperature profile is present. We can further infer that the so-called photovoltaic effect plays only a negligible role. In particular, the photovoltaic effect would only depend on the difference of both Fermi levels of dual-gated graphene junctions. In other words, its sign should change along the diagonals of Fig. 3b,c, which

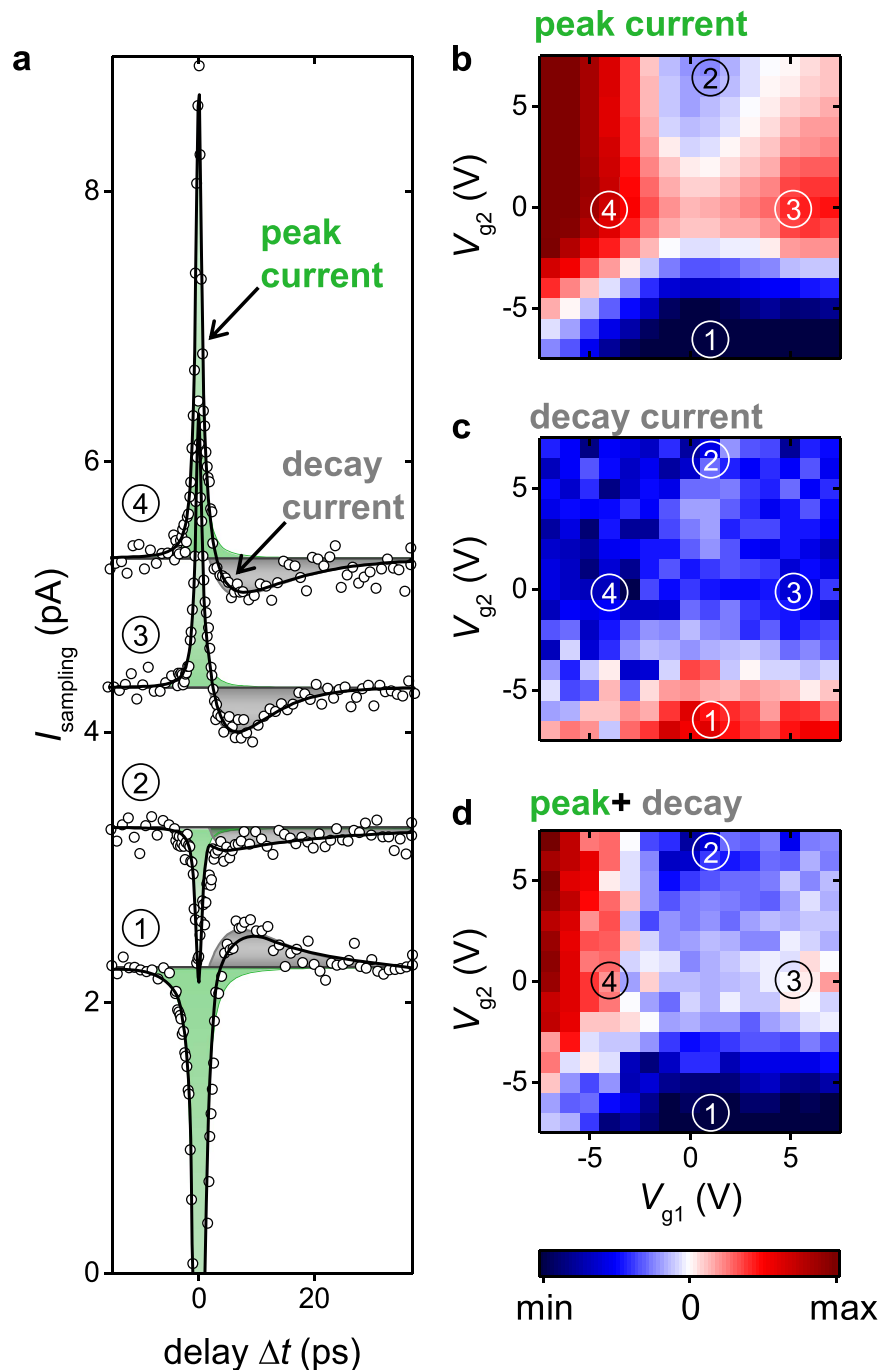


Figure 3. Ultrafast photo-thermoelectric currents in the graphene-junction measured by the THz-circuit.

(a) Time-resolved photocurrent $I_{\text{sampling}}(\Delta t)$ for four different gate voltages at the position $x = y = 0$ (circle in Fig. 1c) with a distinctive ‘peak current’ (green area) and a ‘decay current’ (gray area). (b) Area of the peak current vs. V_{g1} and V_{g2} with the four gate voltage settings 1, 2, 3, and 4 of (a,c). (c) Area of the decay current vs. V_{g1} and V_{g2} . (d) Sum of the areas in figures (b,c).

we do not observe (cf. Supplementary Information). We can also exclude a photo-Dember current^{44,45}, because its amplitude should only depend on the difference of the electron- and hole-mobilities without a sign-change as in Fig. 3b,c. Instead, we demonstrate below that the observed decay current is of thermoelectric origin as well.

Figure 4a–c show the area of the decay current for a time-delay of $3.3 \text{ ps} < \Delta t < 13.3 \text{ ps}$ as a function of both gate voltages for three different excitation positions of the laser spot. The excitation position is varied in steps of $2 \mu\text{m}$ from an excitation position closer to gate1 (Fig. 4a), to one at the center between both gates (Fig. 4b), and to one closer to gate2 (Fig. 4c). We can numerically reproduce the corresponding patterns by Eq. (3) (Fig. 4d,e and f), if we consider a slight shift of the charge neutrality point and an inverted temperature profile (black dots in Fig. 4g,h and i). The shift of the charge neutrality point is induced by the position of the laser spot,

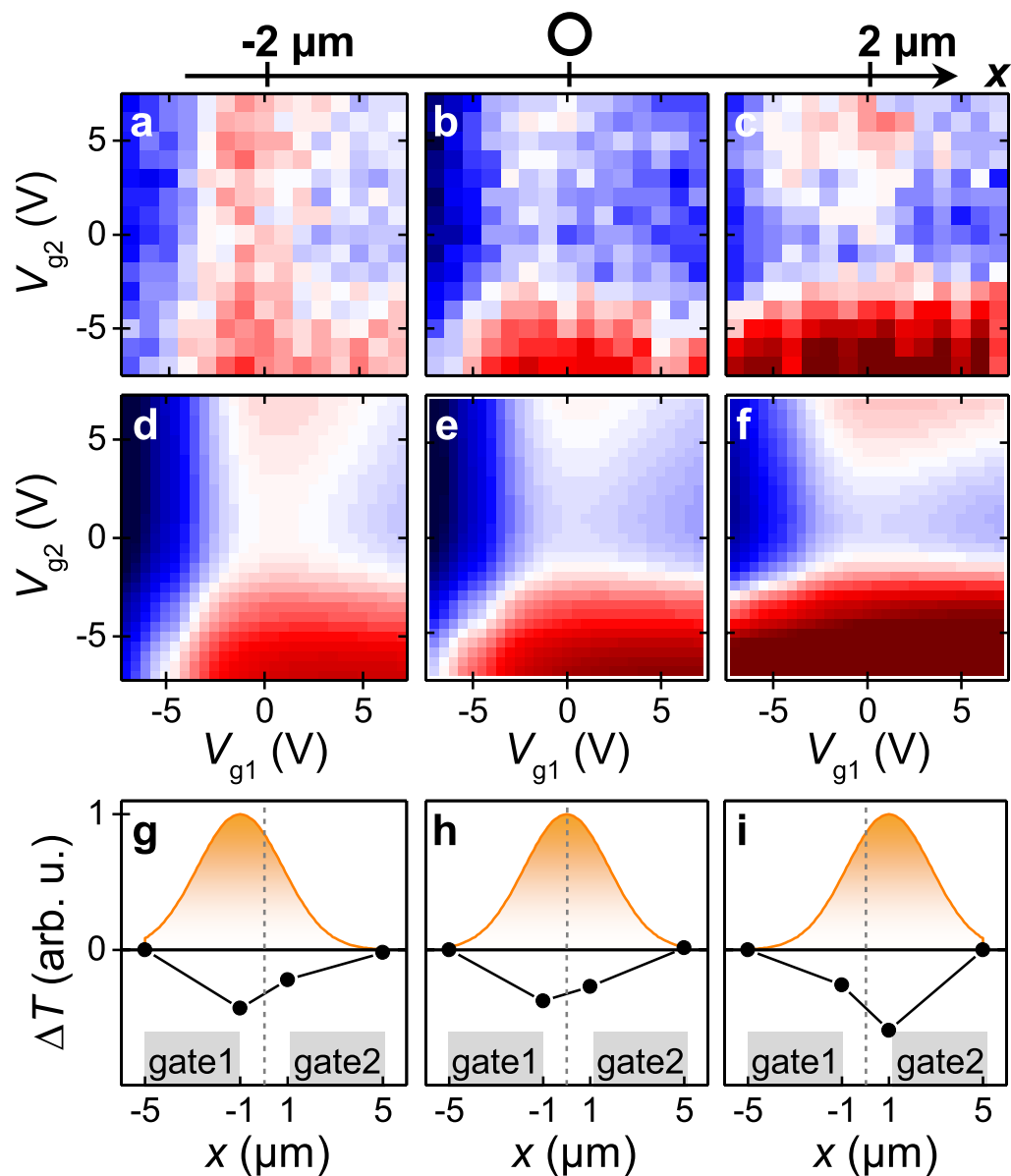


Figure 4. Heat profiling of the graphene-junction. (a–c): Area of the decay current (gray area in Fig. 3a) for three different positions of the laser spot ($x = -2, 0, 2 \mu\text{m}$, and $y = -7 \mu\text{m}$). (d–f): Thermoelectric current calculated for an inverted temperature profile defined in the figure (g,h), and (i). (g–i): Inverted temperature profile (black line) across the graphene junction for time-scales $\Delta t > 1 \text{ps}$. The orange area depicts the Gaussian excitation intensity of the exiting laser pulse, i.e. the initial temperature profile at $\Delta t = 0 \text{ps}$.

because depending on the position, the static, optically induced background doping changes. For instance, the pattern of Fig. 4(a,c) with the laser spot on gate1 (gate2) shows a predominant dependence on V_{g1} (V_{g2}). In other words, the decay current predominantly depends on the voltage of the gate at which the laser is focused. The numerical model (Fig. 4d–f and black data points in Fig. 4g–i) is used to qualitatively mimic both the opposite sign of the decay current compared to the peak current and the shift of the inverted temperature amplitude from gate1 to gate2. To explain the inverted temperature profiles, we need to consider the phonon bath of the graphene. It is heated on a picosecond time-scale by the mentioned electron-phonon scattering processes^{17–19,37–43}. The heat will then be transferred to the environment of the graphene. In the case of the underlying Al_2O_3 -layer and sapphire substrate, this will occur on a 1–10 ps time-scale^{23,41,46}. On this time-scale, the temperature of the electron and phonon baths adopt the same values. In this sense, we interpret τ_{decay} and τ_{rise} of the decay current. For the metal striplines, the heat transfer occurs on a similar time-scale. However, the heat diffusion along the striplines is slower with a time-scale of up to 150–300 ps.⁷ Accordingly, the electron bath in the center of the dual-gated graphene junction efficiently cools-down faster than at the sections which are in vicinity to the metals. In turn, a thermoelectric current is generated with a corresponding longer time-scale at positions closer to one of the

contacts, especially if the contacts are heated by the pump pulse^{7,23}. On the technical side, the detected temporal width of the photo-thermoelectric response in our dual-gated graphene junction is 1.28 ± 0.18 ps. In our interpretation, the detected timescale is limited by the bandwidth limitation of the present stripline circuit³¹, because recently, it was demonstrated by a far-field THz-probe spectroscopy that hot electrons can exhibit a well-defined conductivity up to ~ 1.8 THz in graphene¹⁶. We finally note that both the ‘peak current’ and the ‘decay current’ are detected via our THz-time domain photocurrent spectroscopy. Therefore, both trigger ultrafast optoelectronic signals in the high-frequency circuit, and their polarity can be switched by the two gate voltages of the graphene-junction (Figs 3 and 4).

In conclusion, we show that the ultrafast photocurrent in a dual-gated graphene junction is dominated by the photo-thermoelectric effect. The Fermi energy of the two sides of the junctions is controlled by two adjacent back gates. Surprisingly, we find two distinct ultrafast thermoelectric contributions. A first immediate response occurs within the temporal resolution of our experiment, which is about one picosecond. An unambiguous dependence on the two gate voltages identifies this peak current as an ultrafast photo-thermoelectric current. In our interpretation, this current occurs on a sub-ps time-scale after the pulsed femtosecond laser excitation when the electrons form a hot Fermi Dirac distribution due to fast electron-electron scattering. A second ultrafast thermoelectric response is identified with a decaying constant of a couple of picosecond. We interpret the latter time-scale to represent the heat coupling of the electron and phonon baths to the environment of the graphene. We can numerically reproduce the second response by a thermoelectric current as long as the heat baths are out of equilibrium. The sum of the two time-resolved photocurrent contributions resembles the time-integrated photocurrent measured in the dual-gated graphene junction. The findings may prove essential for graphene-based photodetectors and switches integrated in future high-frequency circuits.

References

- Santos, C. N. *et al.* Terahertz and mid-infrared reflectance of epitaxial graphene. *Sci. Rep.* **6**, 24301 (2016).
- Williamson, I. A. D., Hossein Mousavi, S. & Wang, Z. Extraordinary wavelength reduction in terahertz graphene-cladded photonic crystal slabs. *Sci. Rep.* **6**, 25301 (2016).
- Peters, E. C., Lee, E. J. H., Burghard, M. & Kern, K. Gate dependent photocurrents at a graphene p-n junction. *Applied Physics Letters* **97**, 193102 (2010).
- Xia, F. *et al.* Photocurrent Imaging and Efficient Photon Detection in a Graphene Transistor. *Nano Lett.* **9**, 1039–1044 (2009).
- Xia, F., Mueller, T., Lin, Y., Valdes-Garcia, A. & Avouris, P. Ultrafast graphene photodetector. *Nature Nanotechnology* **4**, 839–843 (2009).
- Park, J., Ahn, Y. H. & Ruiz-Vargas, C. Imaging of Photocurrent Generation and Collection in Single-Layer Graphene. *Nano Lett.* **9**, 1742–1746 (2009).
- Prechtel, L. *et al.* Time-resolved ultrafast photocurrents and terahertz generation in freely suspended graphene. *Nature Communications* **3**, 646 (2012).
- Freitag, M., Low, T., Xia, F. & Avouris, P. Photoconductivity of biased graphene. *Nature Photonics* **7**, 53–59 (2012).
- Gabor, N. M. *et al.* Hot Carrier-Assisted Intrinsic Photoresponse in Graphene. *Science* **334**, 648–652 (2011).
- Lemme, M. C. *et al.* Gate-Activated Photoresponse in a Graphene p-n Junction. *Nano Lett.* **11**, 4134–4137 (2011).
- Song, J. C. W., Rudner, M. S., Marcus, C. M. & Levitov, L. S. Hot Carrier Transport and Photocurrent Response in Graphene. *Nano Lett.* **11**, 4688–4692 (2011).
- Dun, D. *et al.* Ultrafast hot-carrier-dominated photocurrent in graphene. *Nature Nano* **7**, 114–118 (2012).
- Tielrooij, K. J. *et al.* Photoexcitation cascade and multiple hot-carrier generation in graphene. *Nature Physics* **9**, 248–252 (2013).
- Xu, X., Gabor, N. M., Alden, J. S., van der Zande, A. M. & McEuen, P. L. Photo-Thermoelectric Effect at a Graphene Interface Junction. *Nano Lett.* **10**, 562–566 (2010).
- Cai, X. *et al.* Sensitive Room-Temperature Terahertz Detection via Photothermoelectric Effect in Graphene. *Nature Nano* **9**, 814 (2014).
- Jensen, S. A. *et al.* Competing Ultrafast Energy Relaxation Pathways in Photoexcited Graphene. *Nano Lett.*, doi: 10.1021/nl502740g (2014).
- Bistrizter, R. & MacDonald, A. H. Electronic Cooling in Graphene. *Phys. Rev. Lett.* **102**, 206410 (2009).
- Foster, M. S. & Aleiner, I. L. Slow imbalance relaxation and thermoelectric transport in graphene. *Physical Review B* **79** (2009).
- Tielrooij, K. J. *et al.* Generation of photovoltage in graphene on a femtosecond timescale through efficient carrier heating. *Nat Nano* **10**, 437–443 (2015).
- García de Abajo, F. J. Graphene Plasmonics: Challenges and Opportunities. *ACS Photonics* **1**, 135–152 (2014).
- Auston, D. H., Johnson, A. M., Smith, P. R. & Bean, J. C. Picosecond optoelectronic detection, sampling, and correlation measurements in amorphous semiconductors. *Applied Physics Letters* **37**, 371–373 (1980).
- Kastl, C., Karnetzky, C., Karl, H. & Holleitner, A. W. Ultrafast helicity control of surface currents in topological insulators with near-unity fidelity. *Nat Commun* **6**, 6617 (2015).
- Brenneis, A. *et al.* Ultrafast electronic read-out of diamond NV centers coupled to graphene. *Nat Nanotechnology* **10**, 135 (2015).
- Hwang, H. Y. *et al.* Nonlinear THz Conductivity Dynamics in P-Type CVD-Grown Graphene. *J. Phys. Chem. B* **117**, 15819–15824 (2013).
- Frenzel, A. J., Lui, C. H., Shin, Y. C., Kong, J. & Gedik, N. Semiconducting-to-Metallic Photoconductivity Crossover and Temperature-Dependent Drude Weight in Graphene. *Phys. Rev. Lett.* **113**, 056602 (2014).
- Zapata, J. D. *et al.* Efficient graphene saturable absorbers on D-shaped optical fiber for ultrashort pulse generation. *Sci. Rep.* **6**, 20644 (2016).
- Liu, X. M. *et al.* Graphene-clad microfiber saturable absorber for ultrafast fiber lasers. *Sci. Rep.* **6**, 26024 (2016).
- Blaschke, B. M. *et al.* Flexible graphene transistors for recording cell action potentials. *2D Materials* **3**, 025007 (2016).
- Kim, S. *et al.* Realization of a high mobility dual-gated graphene field-effect transistor with Al₂O₃ dielectric. *Applied Physics Letters* **94**, 062107 (2009).
- Cutler, M. & Mott, N. F. Observation of Anderson Localization in an Electron Gas. *Phys. Rev.* **181**, 1336–1340 (1969).
- Prechtel, L. *et al.* Time-Resolved Photoinduced Thermoelectric and Transport Currents in GaAs Nanowires. *Nano Lett.* **12**, 2337–2341 (2012).
- Bao, Q. & Loh, K. P. Graphene Photonics, Plasmonics, and Broadband Optoelectronic Devices. *ACS Nano* **6**, 3677–3694 (2012).
- Avouris, P. & Freitag, M. Graphene Photonics, Plasmonics, and Optoelectronics. *IEEE Journal of Selected Topics in Quantum Electronics* **20**, 72–83 (2014).
- George, P. A. *et al.* Ultrafast Optical-Pump Terahertz-Probe Spectroscopy of the Carrier Relaxation and Recombination Dynamics in Epitaxial Graphene. *Nano Lett.* **8**, 4248–4251 (2008).
- Kim, R., Perebeinos, V. & Avouris, P. Relaxation of optically excited carriers in graphene. *Phys. Rev. B* **84**, 075449 (2011).

36. Sun, D. *et al.* Ultrafast Relaxation of Excited Dirac Fermions in Epitaxial Graphene Using Optical Differential Transmission Spectroscopy. *Physical Review Letters* **101** (2008).
37. Dawlaty, J. M., Shivaraman, S., Chandrashekar, M., Rana, F. & Spencer, M. G. Measurement of ultrafast carrier dynamics in epitaxial graphene. *Applied Physics Letters* **92**, 042116 (2008).
38. Wang, H. *et al.* Ultrafast relaxation dynamics of hot optical phonons in graphene. *Applied Physics Letters* **96**, 081917 (2010).
39. Freitag, M., Low, T. & Avouris, P. Increased Responsivity of Suspended Graphene Photodetectors. *Nano Lett.* **13**, 1644–1648 (2013).
40. Low, T., Perebeinos, V., Kim, R., Freitag, M. & Avouris, P. Cooling of photoexcited carriers in graphene by internal and substrate phonons. *Phys. Rev. B* **86**, 045413 (2012).
41. Graham, M. W., Shi, S.-F., Ralph, D. C., Park, J. & McEuen, P. L. Photocurrent measurements of supercollision cooling in graphene. *Nat Phys* **9**, 103–108 (2013).
42. Betz, A. C. *et al.* Supercollision cooling in undoped graphene. *Nat Phys* **9**, 109–112 (2013).
43. Song, J. C. W., Reizer, M. Y. & Levitov, L. S. Disorder-Assisted Electron-Phonon Scattering and Cooling Pathways in Graphene. *Phys. Rev. Lett.* **109**, 106602 (2012).
44. Erhard, N. *et al.* Ultrafast Photodetection in the Quantum Wells of Single AlGaAs/GaAs-Based Nanowires. *Nano Lett.* **15**, 6869–6874 (2015).
45. Liu, C.-H. *et al.* Ultrafast Lateral Photo-Dember Effect in Graphene Induced by Nonequilibrium Hot Carrier Dynamics. *Nano Lett.* **15**, 4234–4239 (2015).
46. Mak, K. F., Lui, C. H. & Heinz, T. F. Measurement of the thermal conductance of the graphene/SiO₂ interface. *Applied Physics Letters* **97**, 221904 (2010).

Acknowledgements

We thank D. Turchinovich for fruitful discussions. The work was supported by the European Research Council (ERC) Grant NanoREAL (No. 306754).

Author Contributions

A.B. and A.W.H. designed the experiment. A.B., F.S. and A.W. performed the experiments. A.B., F.S., S.D., F.H., H.K., J.A.G. and A.W.H. engineered the materials and the stripline geometry. The manuscript was written through contributions of all authors. All authors have given approval to the final version of the manuscript.

Additional Information

Supplementary information accompanies this paper at <http://www.nature.com/srep>

Competing financial interests: The authors declare no competing financial interests.

How to cite this article: Brenneis, A. *et al.* THz-circuits driven by photo-thermoelectric, gate-tunable graphene-junctions. *Sci. Rep.* **6**, 35654; doi: 10.1038/srep35654 (2016).



This work is licensed under a Creative Commons Attribution 4.0 International License. The images or other third party material in this article are included in the article's Creative Commons license, unless indicated otherwise in the credit line; if the material is not included under the Creative Commons license, users will need to obtain permission from the license holder to reproduce the material. To view a copy of this license, visit <http://creativecommons.org/licenses/by/4.0/>

© The Author(s) 2016